Accepted Article

Senolytic Therapy Enabled by Senescent Cell-Sensitive Biomimetic Melanin Nano-senolytics

Hairui Zhang[1,2,], Xiaoling Xu[1,3,1], Xin Shou[1], Wucan Liao[4], Chengkang Jin[5], Changjiang Chen[4], Chen Zhang[1], Wenhua Gao[4], Junfeng Zhang[4], Weihong Ge[2], Liyun Shi[1,]

[1]Key Laboratory of Artificial Organs and Computational Medicine, Institute of Translational Medicine, Zhejiang Shuren University, Hangzhou, Zhejiang 310015, China.

[2]School of Pharmaceutical Sciences, Zhejiang Chinese Medical University, Hangzhou 310053, China.

[3]Shulan International Medical College, Zhejiang Shuren University, Hangzhou 310015, China.

[4]Department of Immunology and Medical Microbiology, Nanjing University of Chinese Medicine, Nanjing 210046, China.

[5]College of Basic Medical Science, Zhejiang Chinese Medical University, Hangzhou 310053, China.

[*]E-mail: sly0202@zjsru.edu.cn.

Abstract

Cellular senescence is a significant risk factor for aging and age-related diseases (ARD). The canonical senolytics Dasatinib and Quercetin (DQ) have shown promise in clearing senescent cells (SnCs); however, the lack of selectivity poses a challenge in achieving optimal outcomes. Despite the recent occurrence of the nanomaterial-based approaches targeting SnCs, limited therapeutic effects and potential toxicity still remain a major concern. Herein, we developed a "double locks-like" nanoplatform that integrated Galactan coating and mesoporous polydopamine to encase the senolytic drug DQ. By this way, DQ was only released in SnCs that were featured with higher levels of β-galactosidase (β-gal) and low PH. Additionally, the nanoparticles were equipped with 2,2,6,6-Tetramethylpiperidine-1-oxyl (Tempo) to gain enhanced photothermal converting potential. Consequently, the synthesized nanosenolytics demonstrated remarkable specificity and efficacy in eradicating SnCs, and accordingly reversed pulmonary fibrosis in mice without affecting normal tissues. Upon exposure of near-infrared (NIR) light, the nanoparticles demonstrated to efficiently remove senescent tumor cells inducted by chemotherapy, thereby hindering the outgrowth and metastasis or breast cancer. Collectively, the present study develops an "On/Off" switchable nanoplatform in response to SnCs, and produces a more safe, efficient and feasible way to delay aging or alleviate age-associated diseases.

Keywords

Dasatinib and Quercetin; Pulmonary fibrosis; breast cancer; β-galactosidase; Targeting senescent cells; "On/Off" switchable nanoplatform.

Graphical Abstract

Schematic illustration of the synthesis and therapeutic process of Gal-TMPDA@DQ.

1. Introduction

The rising in the aging population has become a common pheromone all over the world, and it is estimated to have at least 2.1 billion people over 60 years old by 2030 [1]. Since advanced age is considered as a major risk factor for various degenerative and chronic diseases, it is imperative to develop the anti-aging therapies or preventions on the basis of hallmarks of aging. Cell senescence has been recognized as a major signature, as well as a fundamental cause of the organismal aging [2]. Cellular senescence is a cell state characterized by replicative arrest, highly expression of cell cycle-related inhibitory proteins such as P53, P21 and P16, increased senescence-associated β-galactosidase (SA-β-gal) level, and production of a plethora of proinflammatory cytokines, chemokines and extracellular matrix-degrading proteases, which is known as senescence-associated secretory phenotype (SASP). Through the SASP, senescent cells (SnCs) induce sterile inflammation, tissue damage, fibrotic pathogenesis and senescence of bystander cells. Accordingly, pathologic accumulation of SnCs would lead to a range of age-associated disorders such as cancer, pulmonary fibrosis, cardiovascular disease, neurodegenerative disorders and exacerbated viral infection [3].

Due to the central place for SnCs in age-related pathologies, elimination of SnCs has emerged as a plausible therapeutic strategy to prevent, delay, or alleviate the immediate or long-term health impacts posed by the aging process [4]. Senolytics are a class of compounds that can eradicate SnCs by inducing cellular apoptosis and programmed cell death. Recently, an expanding list of senolytic agents, such as combination of Dasatinib and Quercetin (DQ) [5], BCL inhibitors ABT-263/737 [6], HSP90 inhibitors [7], Cardiac glycosides [8] and procyanidin C1 [9] have been discovered and show the SnC-clearing effects. Among them, DQ is the first identified, and also the most characterized senolytic drug. Dasatinib is an FDA-approved tyrosine kinase inhibitor able to induce apoptosis in SnCs by inhibiting the Src tyrosine kinase. Quercetin is a naturally occurring flavonoid with the ability to induce cell

apoptosis through repressing the anti-apoptotic molecules such as BCL-xL. Studies have shown that combination of dasatinib and quercetin exerted significant effects in the elimination of SnCs and the relief of SASP in various tissues [3a, 10]. Accordingly, DQ has been tested to treat the aging-related diseases such as atherosclerosis [11], senile osteoporosis [12], diabetic kidney disease [13] and type II diabetes [14]. Recently, two clinical trials were approved to apply the senolytic DQ to treat idiopathic pulmonary fibrosis (IPF), which showed the promising outcome in improving patients' physiology, though the examination of entailing larger population of participants and the evaluation of long-term effects are needed [15]. Despite the progress made in the application of senolytic therapy (senotherapy), emerging evidences indicate that critical issues, such as low selectivity, limited therapeutic potency and potentially off-target effects, hamper its further implementation [16]. In particular, studies have reported that DQ exerted the non-specific cytotoxic effects, and displayed no selectivity toward senescent human fibroblasts [6, 17]. As proof-of-concept evidences, treatment with DQ demonstrated 55% cytotoxicity in non-senescent cells (NSs) at higher doses [18]. Administration of Dasatinib was shown to cause thrombocytopenia [19], lung vascular toxicity and even pulmonary hypertension [20]. Furthermore, the data from clinical trials revealed that a series of adverse events including feeling unwell, cough, nausea, fatigue, weakness, and headache were observed in IPF patients with the senotherapy, which might ultimately impede compliance with the DQ therapy. Another concern is the limited efficacy of the senolytics to clear SnCs and improve the age-related pathologies [21]. It was reported that high dose of DQ was required for optimized therapeutic effect [22], which however would be harmful to normal cells. Additionally, the agents demonstrate incomplete absorption, high first-pass metabolism, and low bioavailability [23]. Thus, the challenges current senotherapy facing call for the innovative senolytic system with improved selectivity, efficacy and biosafety.

The nanomaterial-based drug delivery system provides one of the most effective and accessible platforms to overcome these problems. Polydopamine (PDA) is a natural melanin-like biopolymer with excellent biocompatibility, biodegradability, PH responsiveness and photothermal conversion properties, making it an ideal nano basis for controlled delivery of senolytics [24]. Moreover, the mesoporous framework with adjustable channel endows the mesoporous PDA (MPDA) with high drug loading capacity and sustainable drug release properties, allowing efficiently send and release the senolytics at targeted tissues avoiding drugs diffusion [25].

Cell-targeted drug delivery systems can significantly enhance the intracellular accumulation and controlled release of senolytics in aged tissues over health ones. The challenged work is to distinguish SnCs from normal cells. In recent years, a spectrum of biomarkers targeting SnCs have been identified to differentiate them from non-senescent cells. Among them, the molecules such as integrin $\alpha v\beta 3$ and uPAR have been applied to develop the SnC-specific nano therapies [26], which showed the potential in the treatment of a wide range of age-related diseases. By exploiting the ever-increasing SnC-specific targets, the senolytics drugs can be more efficiently and specifically delivered to the aged cells or tissues for inducing cell apoptosis and mitigating SASP secretion, and thereby resuming tissue homeostasis and rejuvenating the organisms. In addition, the increased lysosomal SA-β-gal level has been appreciated as a hallmark of cellular senescence, and its activity can be detected in the organs of old individuals and animals. For these reasons, SA-β-gal has been widely used to identify SnCs and to specifically target SnCs for their elimination, essentially by taking advantage of a galactose-modified surface layer [27]. Currently, researchers have developed a series of prodrugs that can be cleaved by β-Gal [27a, 28]. By this, the responsive moieties act as the protective "locks" in normal cells to prevent the side-

effects of the senolytic drugs, while β-Gal in senescent cells functions as a specific "key" to release the effector molecules and enable targeted drug delivery and treatment.

Additionally, considering that multiple biological pathways are involved in age-associated pathology, it is expected that monotherapy may not achieve the successful efficacy in elimination of SnCs. An innovative approach integrating canonical senolytics and the nano therapy such as photothermal therapy (PTT) might have additive benefits to clear SnCs and elevate the therapeutic potential, especially in treating the refractory cancers that undergo the senescent transition induced by chemotherapy [29].

To overcome the limitations associated with current senotherapy, we herein developed a multifunctional nanomaterial based on mesoporous polydopamine (MPDA), which provided a platform for efficient encapsulation and controlled release of the senolytic cocktail DQ. Unlike the traditional β-Gal-based "lock-and-release" method, we implemented a "dual-lock" approach that consists of a Galactan-modified layer and TMPDA. Upon entry of the nanocarrier into SnCs and subsequent engulfment by lysosomes, the "first lock" of our nanosenolytics is triggered and deblocked. By exploiting the lower PH in SnCs, TMPDA is activated and unlock the "second lock" of the senolytics. Only when both "locks" are successfully opened, DQ can be released into the aged cells. As such, the synthesized nanosenolytics, termed Gal-TMPDA@DQ, demonstrated to specifically and efficiently eradicate SnCs with no evident effects on normal cells. Consequentially, treatment of the nanosenolytics greatly improved pulmonary fibrosis, and inhibited cancer progression post chemotherapy. We thus developed a novel senotherapy with improved selectivity, efficacy and biosafety, which shows a promising to treat age-related diseases.

2. Results

2.1. Preparation of Gal-TMPDA@DQ

To increase the selectivity and efficacy of the senolytic treatment, we established a polydopamine nanoparticles-based nanoplatform that enclosed a well-appreciated senolytic cocktail DQ. PDA has demonstrated the promise in early diagnosis and targeted drug delivery owing to its biocompatibility, biodegradability, and photothermal conversion, but its encapsulation efficiencies of hydrophobic drugs was unsatisfied. We thus developed the MPDA polymers by mixing the F127, P123, DA oligomers, and 1,3,5-trimethylbenzene (TMB) with ammonium hydroxide as the catalyst. Additionally, Tempo, a nitroxyl radical with enhanced photothermal conversion capability [30], was doped onto the PDA to fabricate the polymers, namely TMPDA.

Afterwards, the senolytic agents D and Q were loaded onto the mesoporous particles to generate a stable and biocompatible drug carrier. A layer of Galactan (Gal), which was presumably catalyzed by SA-β-gal, was subsequently synthesized and encapsulated the nanospheres. As such, the synthesized nanoparticles, termed Gal-TMPDA@DQ, were expected to response to the enzymes in senescent cells and release the senolytics for specific killing. Moreover, the incorporation of Tempo endowed the polymers with enhanced light absorption, and photothermal activity to maximize the therapeutic effects.

2.2. Characterization of Gal-TMPDA@DQ

We then characterized the nanoparticle. Dynamic light scattering (DLS) examination revealed that the size of Gal-TMPDA@DQ was 147.20 ± 22.17 nm, with Gal-MPDA@DQ at 155.13 ± 25.58 nm (Figure 1A, B). Compared with bare TMPDA (108.83±16.37 nm) and MPDA (126.57±19.07 nm), the particle size of DQ-incorporated nanoparticles was slightly increased, which may be due to the loading of DQ and the encapsulation of Galactan (Figure S1A and S1B, Supporting Information). The polymers maintained stable during the tested period of 96 h, as no significant alterations were observed in the particle's sizes and

polydispersity (Figure 1C, D) (Figure S1C and S1D, Supporting Information). Transmission electron microscopy (TEM) revealed that the mesoporous particles were decorated with the spheroid-like nanochannels with the diameters of approximately 26.03±6.43 nm (Figure 1E). Zeta potential analysis demonstrated that the nanoparticles were measured as -19~-16 mV (Figure 1F).

Next, we set to assess the encapsulation efficiency (EE) and the drug loading (DL) of Gal-TMPDA@DQ. The results showed that the EE values for D and Q were 90.39 ± 0.91% and 87.91 ± 2.87%, respectively, and the DL values were at 18.08±0.18 μg/mg and 45.71±1.50 μg/mg, respectively (Figure 1G). Since D and Q doped at the nanoparticles were expected to be released at acid lysosomes upon the catalyzing effect of β-Gal when the particles were internalized in SnC, we therefore established an acid (PH 5.5) culture system with the addition of β-Gal to test the in vitro release of drugs. Ultra-high-performance liquid chromatography (UHPLC) revealed that, in the absence of β-Gal, the release rates of D and Q were only 33.6% and 26.6% respectively within 48 h, whereas the addition of β-Gal caused cleavage of the Galactan layer at the nanospheres and release of D and Q at the increased rates 69.12% and 50.08%, respectively. Interestingly, we observed that near-infrared irradiation (NIR 808 nm; 1.5 W/cm^2) further boosted the drugs release, and induced the D and Q release at the rates of 77.98% and 63.96%, respectively (Figure 1H, I). This effect might be attributed to the photothermal properties of TMPDA, as it was able to generate the heat under NIR, which in turn caused the disruption of hydrogen bonds between DQ and TMPDA, and thereby promoted the drugs release. We additionally performed Molisch test, a straightforward method for detecting carbohydrates [31], to confirm the interaction of β-Gal with the Galactan at the nanoparticles. The results showed that Gal-TMPDA@DQ induced a positive reaction in the presence but not the absence of β-Gal, further supporting the decomposition of the Galactan layers by β-Gal (Figure 1J).

Next, we assessed the photothermal conversion effect of TMPDA-integrated senolytics. To this end, the ability of Gal-TMPDA@DQ to absorber the light (808 nm, 1.5 W/cm^2, 300 s) to convert the heat (temperature) was measured using a radiation thermometer system. The results showed that while ddH$_2$O and Free DQ maintained the tested system at room temperature, Tempo-dotted MPDA caused a remarkable rise in temperatures (Figure 1K). Interestingly, we found that loading of DQ to TMPDA micelles caused a slight decrease the temperature, likely due to their structures or chemical properties. The data also demonstrated that TMPDA emitted the heat energy in time- and dose-dependent manner (Figure 1L). We also observed a good correlation between the NIR power densities and the elevated temperatures, indicating the thermoresponsive capability of the TMPDA moiety (Figure 1M). Additionally, Tempo-dotted MPDA maintained photostability following repeated NIR irradiation (Figure S1E, Supporting Information). According to the plot of time versus negative natural logarithm of the temperature driving force ($\Delta T/\Delta T_{max}$) in the natural cooling process, the value of τ (τ= 164.04) was obtained, and the photothermal conversion efficiency of TMPDA was calculated to be 37.55% (Figure 1N). Thus, the data indicated that Gal-TMPDA@DQ could effectively convert NIR energy into heat to achieve PTT in targeted cells.

In addition, we conducted a hemolysis assay to test whether the synthesized nanomaterial would cause blood cell disruption at physiological PH (7.4). The results showed that the hemolysis rate of Gal-TMPDA@DQ was negligible, and no evident phagocytosis and aggregation of negatively charged blood cells were observed (Figure S1F and S1G, Supporting Information). Collectively, our data indicated that the MPDA-based polymers that integrated the senolytic agents DQ, SnC-targeting Galactan layers, and Tempo moiety were successfully synthesized**.**

2.3. In-vitro elimination of senescent cells

Pulmonary fibrosis is an age-associated disease characterized by the accumulation of senescent cells. Studies have shown that progressively aging of alveolar type II (ATII) epithelial cells is an early and critical event that underpins lung aging and fibrosis [32]. We thus set out to explore whether Gal-TMPDA@DQ could selectively eliminate senescent lung cells to modulate pulmonary fibrosis. For this, an ATII epithelial cell line, A549 cells, were incubated with Bleomycin (Bleo), an agent proposed to cause pulmonary fibrosis and senescence of alveolar epithelial cells [33]. Expectedly, treatment of A549 cells with Bleo (0.01 U/ml) for 2 days elicited a series of senescent markers such as intensified SA-β-Gal staining (Figure S2A, Supporting Information). Moreover, elevated expression of TGF-β, SMAD2, and ITGAV (Figure S2B, Supporting Information), similar to ATII epithelial cells, was observed [34], which is highly reminiscent of the occurrence of IPF. Subsequently, we examined whether the nanoparticles could specifically target SnC by applying the Nile Red-labeled polymers, which were then incubated with either senescent A549 or control cells. Co-localization of Nile Red (NR) and the cell nucleus (DAPI) was detected at different time points (0, 2, 4, 6, and 12 h post incubation) (Figure 2A). The results showed that the fluorescence intensity of Nile Red was significantly higher in senescent cells than that in normal cells (Figure 2C), and the flow cytometry analysis confirmed this trend. The data thus supported the preferential internalization of the nanoparticles by SnCs (Figure 2B).

Next, we sought to define the intracellular localization of Galactan-modified TMPDA nanospheres in SnCs by exploiting the commercial staining dyes that specifically labeled lysosomes. Co-localization examination revealed a remarkable overlay of the NR fluorescence (Gal-TMPDA@NR) with Lyso-Tracker in senescent A549 cells (Figure 2D, E). Thus, the data indicated that the nanoparticles were preferentially taken up by SnCs and essentially accumulated in lysosomes, allowing subsequent β-gal-mediated enzymatic reaction.

We then proceed to test the senolytic activity of the prepared polymers in normal or aged A549 cells. We firstly demined a relatively safe dose of Gal-TMPDA@DQ (100 µg/ml) that exerted marginal effect on the viability of normal cells (Figure 2F). However, such dose of the nanosphere caused a significantly increased senolytic activity (62%), compared with that of Free DQ (38%) (Figure 2G). In line, the Annexin V-FITC/PI staining, a well-established approach for measuring cellular apoptosis, revealed that Gal-TMPDA@DQ elicited a higher apoptosis rate (71.6%) than Free DQ (40.3%) in SnC. Among them, Free DQ also induced apoptosis in normal cells (23%), which was eliminated in Gal-TMPDA@DQ. In parallel, Gal-TMPDA@DQ treatment caused a profound reduction in the levels of senescent markers including SA-β-gal, p53, p21 in senescent A549 cells, as compared with Free DQ administration (Figure 2H, I). Together, the results indicated that Gal-TMPDA@DQ were efficiently internalized by SnC and targeted lysosomes to exert the specific and potent senolytic effects via co-opting Galactan.

2.4. Gal-TMPDA@DQ exhibits better effects than Free DQ in mitigating bleomycin-induced lung injury

The above findings promoted us to further assess the senolytic activity of Gal-TMPDA@DQ. For this, we established a Bleo-induced mice model of IPF, a well-recognized model related with lung aging and cellular senescence [35]. Firstly, we examined the tissue distribution of the nanoparticles in mice following Bleo administration. The results demonstrated that the NR-incorporated particles, upon injection via tail veins, efficiently migrated into the lung particularly at 12 h post inoculation (Figure 3A and figure S3A, Supporting Information). This was likely due to the SnC-targeting activity of the nanoparticles, and set a basis for subsequent therapeutic effects. We then assessed the impact of the nanoparticles on lung pathologies in fibrotic mice (Figure 3B). Remarkably, the data demonstrated that a profound loss in body mass induced by Bleo treatment was substantially mitigated by Gal-

11

TMPDA@DQ relative to Free DQ treatment (Figure 3C, D). H&E staining of lung sections revealed severe lung pathologies upon Bleo administration, characterized by thickening of alveolar walls and disruption of alveolar structure, which was significantly improved by Gal-TMPDA@DQ, to a greater extent than Free DQ treatment (Figure 3E). Next, we detected the content of hydroxyproline, a cardinal feature of pulmonary fibrosis, and found that its level was significantly decreased in the lung tissues of mice treated with Gal-TMPDA @ DQ, when compared with that of lungs in Free DQ-treated group (Figure 3F). Also, Masson staining and immunofluorescence staining demonstrated that the collagen deposition (Figure 3G, H) and α-SMA level (Figure 3I, J) were reduced by DQ treatment in fibrotic mice, but was more profoundly lessened by Gal-TMPDA@DQ administration. Together, the results demonstrated a superior function of Gal-TMPDA@DQ, compared with Free DQ, in alleviating Bleo-induced lung fibrosis in mice.

2.5. Gal-TMPDA@DQ specifically removes SnCs in IPF mice

We next sought to address whether the protective effects of Gal-TMPDA@DQ were related with its senolytic activity. Notably, the data showed that the percentages of β-Gal$^+$ SnC was greatly reduced by Gal-TMPDA@DQ relative to Free DQ treatment in lungs of fibrotic mice (Figure 4A, C). The staining of senescence-associated γH2AX foci, indicative of senescence, was also more significantly reduced by Gal-TMPDA@DQ treatment (Figure 4B). Additionally, the levels of the senescence-related factors in lung tissue such as P53, P21, and P16 (Figure 4D) as well as inflammatory factors in bronchoalveolar lavage fluid (BALF) such as IL-1β, IL-6, IL-10 and TNF-α (Figure 4F) were substantially reduced by Gal-TMPDA@DQ treatment compared with that upon Free DQ treatment. Heatmap analysis also indicated that Gal-TMPDA@DQ treatment markedly reduced the levels of SnC-associated genes in fibrotic lungs (Figure 4E). Collectively, our data indicated that compared Free DQ,

Gal-TMPDA@DQ exhibited more potent roles in clearing SnCs, reducing senescence-associated features, and thereby mitigated lung pathologies and promoting tissue integrity.

2.6. Gal-TMPDA@DQ exhibits no significant tissue toxicity

Canonical senolytics have shown the promising in eradicating SnCs but they may also kill non-senescent cells and cause the off-target effects due to their inability to recognize SnCs [15a, 212, 36]. We thus further evaluated the potential toxic effects caused by the nanosenolytics. Indeed, H&E staining of tissue slices revealed that no significant tissue damages were induced by the nanoparticles in major organs in heart, liver, spleen, and kidney (Figure 5A). A complete blood count indicated that there were no marked alterations in the counts of white blood cell (WBC), red blood cells (RBC), and platelet (PLT), as well as the level of hemoglobin (HGB) in mice receiving the nanotherapeutics (Figure 5B-E). Also, the nanoparticles treatment caused no significant effects on the levels of alanine transaminase (ALT) and aspartate transaminase (AST), the typical biomarkers of liver function, and on the concentration of blood urea nitrogen (BUN), an indicator of kidney function (Figure 5F-H). Thus, our data indicated that Gal-TMPDA@DQ and the associated nanomaterials displayed good biocompatibility with no significant tissue toxicity.

2.7. Gal-TMPDA@DQ effectively eliminates chemotherapy-induced senescent cancer cells

Conventional anticancer treatments such as chemotherapy have been proved to induce senescence in cancer cells, which may potentially cause cancer dormancy, therapy evasion and a risk for tumor relapse [37]. Palbociclib (Pab) is a drug used for the treatment of advanced estrogen-receptor-positive breast cancer, and it is also a selective inhibitor of cyclin-dependent kinases 4 and 6 (CDK4/6) that induces cell cycle arrest and senescence. We thus extended our study to analyze whether the nanosenolytics could remove senescent

cancer cells that were induced by chemotherapies such as Pab. Initially, our data demonstrated that treatment of breast cancer cells, 4T1 cells, with 5 µM Pab for 14 days [38] elicited 70% β-Gal$^+$ SnC, along with elevated expression of p53, indicative of SnCs induced by Pab treatment (Figure 6A, B). Next, using the NR-labeling approach, we demonstrated that the TMPDA nanoparticles were preferentially taken by Pab-induced senescent 4T1 cells (Figure 6C-E). Accordingly, Gal-TMPDA@DQ (100 µg/ml) caused 60% cell death in SnCs, while exerting not significantly effect on non-senescent cells. Moreover, combination of Gal-TMPDA@DQ with near-infrared irradiation (NIR) led to about 83% cell death, whereas Free DQ treatment only elicited 41% cell apoptosis (Figure 6H, I). The results thus indicated that Gal-TMPDA@ DQ selectively targeted senescent cancer cells, and combined with the irradiation, to exert much more potent effects than Free DQ to remove SnCs.

2.8. Gal-TMPDA@DQ is accumulated in senescent tumor tissues

To further confirm SnC-targeting properties of the nanoparticles, we then established a breast cancer model by injecting 4T1 cells into the mammary fat pad of BALB/c mice, and Pab was administrated from day7 once every day for one week. As expected, Pab treatment caused a remarkable SA-β-Gal staining and reduced immunostaining of Ki67 in tumor tissues, indicative of cell cycle arrest and senescence (Figure 7A, B). Next, we examined whether the nanoparticles could be able to migrate to the senescent tumor tissues when injected intravenously. Remarkably, the results showed that NR-labeled Gal-TMPDA particles rapidly trafficked into the breast tumor sites in Pab-treated mice, peaked at 24 h post inoculation (Figure 7C-E). Nevertheless, no significant signals were detected in tumors without pretreatment of Pab, further supporting the SnC-targeting activity of the nanoparticles.

In addition, considering the thermoresponsive capability of Tempo, we measured the temperature at the tumor site of tumor-bearing mice by exploiting a photothermal imaging system. The results demonstrated that Gal-TMPDA@DQ treatment caused a rapid rise of the tumor temperatures, up to 61.5 °C after 3 min of laser irradiation, whereas Gal-MPDA@DQ caused the temperature rising to 47.9 °C (Figure 7F). Combined with that above observation about the enhanced senolytic activity (Figure 6G), the data indicated that the incorporation with Tempo endowed the nanomaterials with additive effects to more efficiently kill cancer cells.

2.9. Gal-TMPDA@DQ/R cooperating with Pab significantly inhibits tumor growth

Encouraged by the above observations, we then explored the potential role of the nanoparticles, by co-acting with the chemotherapeutic agents, in treating refractory cancers. For this, the breast cancer 4T1 cells were injected into the mammary fat pads of BALB/c mice, followed by Pab administration 7 d later. Also, Free DQ or the synthesized nanparticles were applied from at day15, 18, 21. To maximize the effects of the thermosensitive Tempo, the mice also received the irradiation one day the nano therapy (Figure 8A). During the whole tested period, we observed no significant alterations in body weight among groups of mice (Figure 8B). Treatment of Pab retarded tumor growth, but with weaker effects compared with that induced by cooperation of Pab with Free DQ, or Gal-modified TMPDA@DQ. More strikingly, Gal-TMPDA@DQ combined with irradiation displayed much more effects in impeding tumor growth, and even completely eradicated tumors (Figure 8C, D).

In addition, we evaluated the in vivo senolytic effect of various treatments. TUNEL analysis of tumor tissue sections demonstrated that, compared with Free DQ treatment, Galactan-conjugated TMPDA@DQ exerted more profound effects in inducing cellular

15

apoptosis, particularly when collaborating with the irradiation (Figure 8E). Congruently, H&E staining revealed that Pab treatment only caused slight nuclear enlargement and dissolution in tumor cells, while combination of the senolytics, especially Gal-TMPDA@DQ/R, led to severe cellular apoptosis, characterized by nuclear pyknosis, karyorrhexis, and karyolysis (Figure 8F). Thus, the data consistently supported the enhanced tumoricidal activity of Galactan-modified senolytics, and Tempo-mediated thermal activity boosted the therapeutic effects.

In addition, we evaluated the potential tissue toxicity of the nanomaterials, and found no significant damages were caused in major organs such as hearts, kidney, liver, spleen and blood cells (Figure S4, Supporting Information). In the investigation of tissue toxicity in various organs, we observed the aggregation of tumor cells in the lungs, indicating the occurrence of lung metastasis in breast cancer. Consistently, lung metastasis of breast cancer was inhibited by combinative treatment of Pab with DQ, but with more profound effects upon combination with Gal-TMPDA@DQ and NIR irradiation (Figure 8G). Together, the findings indicated the nanotherapeutics integrated multiple mechanisms involving SnC-targeting, specific killing and PTT behaviors, to maximize anti-tumor therapeutic effects and limit unwanted tissue damage.

Figure. 1. Characterization of Gal-TMPDA@DQ. Hydrodynamic size distribution of (A) Gal-MPDA@DQ and (B) Gal-TMPDA@DQ at 0h by DLS. (C) Hydrodynamic size changes of Gal-MPDA@DQ and Gal-TMPDA@DQ at 0, 4, 8, 24, 48 and 96 h by DLS. (D) The polydispersity of Gal-MPDA@DQ and Gal-TMPDA@DQ at 0, 4, 8, 24, 48 and 96 h by DLS. (E) TEM images of MPDA, Gal-MPDA@DQ, TMPDA and Gal-TMPDA@DQ (scale bar = 200 nm). (F) Zeta potential of MPDA, TMPDA, Gal-MPDA@DQ and Gal-TMPDA@DQ. (G) The

encapsulation efficiency (EE) and drug loading (DL) of D and Q in Gal-TMPDA@DQ. The release of (H) D and (I) Q from Gal-TMPDA@DQ at PH 5.5 or PH 5.5/β-Gal or PH 5.5/β-Gal/NIR. (J) The Molisch reaction of Gal-TMPDA@DQ. (K) The temperature curves of the solution containing the indicated agents following exposure of NIR (808 nm; 1.5 W/cm^2) for 300 s. (L) The temperature curves of the solution containing TMPDA at the indicated concentrations following exposure of NIR (808 nm; 1.5 W/cm^2) for 300 s. (M) The temperature curves of TMPDA solution (100 μg/ml) subjected to NIR at the indicated intensities for 300 s. (N) The temperature curves of TMPDA solution (100 μg/ml) under NIR (808 nm, 1.5 W/cm^2) for the indicated time periods. Inset: plot of time versus negative natural logarithm of the temperature driving force ($\triangle T/\triangle T_{max}$) in the natural cooling process. (O) Infrared thermal images of Gal-TMPDA@DQ solution at the indicated concentrations subjected to NIR irradiation (808 nm, 1.5 W/cm^2) for the time periods as indicated. Data are from 3 experiments and presented as means ± SD. * $P < 0.05$, ** $P < 0.01$, *** $P < 0.001$, **** $P < 0.0001$.

Figure. 2. Gal-TMPDA@DQ is preferentially taken by SnCs for specific killing. (A) Confocal images of normal and senescent A549 cells (Bleo-pretreated) incubated with Nile red (NR)-loaded Gal-TMPDA (50 μg/ml) for the indicated time periods. Nuclei, DAPI (scale bar = 50 μm). (B) Flow cytometric analysis of normal and senescent A549 cells (Bleo-pretreated) incubated with Gal-TMPDA@NR, and (C) the fluorescence intensities were shown of confocal images. (D-E) Confocal fluorescence images showing the subcellular localization of Gal-TMPDA@NR in Bleo-induced senescent A549 cells and cross-sectional analysis. Lysosome, Lyso tracker; Nuclei, DAPI. Scale bar = 10 μm. (F) The viability of normal A549 cells incubated with Gal-TMPDA@DQ at the indicated concentrations for 24 or 48 h. (G-K) Normal or senescent A549 cells were incubated with the indicated agents for 24 h (Free DQ

(D: 2.87 µM, Q: 17.20 µM), MPDA (MPDA:100 µg/ml), TMPDA (TMPDA:100 µg/ml), Gal-MPDA@DQ (MPDA:100 µg/ml, D: 2.87 µM, Q: 17.20 µM) and Gal-TMPDA@DQ (TMPDA:100 µg/ml, D: 2.87 µM, Q: 17.20 µM). The viability of senescent A549 cells (G), protein levels of p53 and p21 (H), SA-β-Gal staining (scale bar = 50 µm) (I), flow cytometry of cell apoptosis (J) and quantitative analysis (K). Data are from 3 experiments and presented as means ± SD. * $P < 0.05$, ** $P < 0.01$, *** $P < 0.001$, **** $P < 0.0001$.

Figure. 3. Gal-TMPDA@DQ alleviates bleomycin-induced lung fibrosis. (A) Mice were intratracheally instilled with bleomycin (2 U/kg) or saline for two weeks, and Nile red (NR)-loaded Gal-TMPDA (5 mg/ml, 200 µl) were instilled via tail veins and traced by IVIS system (Color Scale: Min =1.94e8, Max =2.41e9) at the major organs at the indicated time periods post nanoparticles injection (n= 3). (B-I) The simplified experimental scheme. C57BL/6J mice were intratracheally instilled with bleomycin for 6 days, and then divided randomly for 5 groups for treating with free DQ (D: 0.7 mg/kg, Q: 2.6 mg/kg), MPDA (5 mg/ml, 200 µl), TMPDA (5 mg/ml, 200 µl), Gal-MPDA@DQ (MPDA: 5 mg/ml, D: 70 µg/ml, Q: 260 µg/ml, 200 µl) or Gal-TMPDA@DQ (TMPDA: 5 mg/ml, D: 70 µg/ml, Q: 260 µg/ml, 200 µl). Mice were sacrificed 24 days after bleomycin injection, and blood, bronchoalveolar lavage fluid (BALF), and major organ sections were collected for analysis (B). The changes of body weights (n= 8) (C); final weight level (n= 8) (D); H&E staining of lung tissues, Scale bars, 1 mm and 100 µm (n= 3) (E); hydroxyproline content in lung tissues (n= 5) (F); Masson staining of lung tissues. Scale bar, 100 µm (n= 3) (G), and quantification of Masson staining of collagens (n= 3) (H). Immunofluorescence staining of α-SMA in lung tissues. Nuclei, DAPI. Scale bar = 50 µm (n= 3) (I), and quantification of α-SMA levels in lung tissue sections (n= 3) (J). Data are presented as means ± SD. * $P < 0.05$, ** $P < 0.01$, *** $P < 0.001$, **** $P < 0.0001$.

Figure. 4. Gal-TMPDA@DQ reduces the senescent markers by removing SnCs in fibrotic mice. The fibrotic mice model was established and subjected to the naontherapies as described in Figure 3B. (A) Representative images showing SA-β-Gal staining of lung tissue sections (scale bar = 50 μm) (n= 3), and (C) quantification of SA-β-Gal staining (n= 3); (B) Representative images showing γ-H2AX staining of lung tissue sections (scale bar = 20 μm) (n= 3); (D) Levels of senescence-related proteins determined by Western blotting (n= 3); (E) Heatmap analysis of the expression of age-related genes in murine lungs (n= 3); (F) The BALF level of SASP cytokines including IL-1β, IL-6, IL-10 and TNF-α (n= 6). Data are presented as means ± SD. * $P < 0.05$, ** $P < 0.01$, *** $P < 0.001$, **** $P < 0.0001$.

Figure. 5. Gal-TMPDA@DQ exhibits excellent biocompatibility during treating mice. The fibrotic mice model was established and subjected to the naontherapies as described in Figure 3B. (A) H&E staining of major organs (heart, liver, spleen, kidney). Scale bar = 200 μm) (n= 3); (B-H) Complete blood analysis for blood cell counts (HBG, PLETs, RBCs and WBCs), and factors related with liver (ALT, AST) and kidney (BUN) function (n= 6). Data are presented as means ± SD. Shown are representative images.

Figure. 6. Gal-TMPDA@DQ is taken by senescent cancer cells to mediate senolytic activity. (A) The SA-β-Gal staining of 4T1 cells with or without Pab treatment. Scale bar = 50 μm. (B) The protein levels of p53 in 4T1 cells with or without Pab treatment. (C) Confocal images showing the internalization of Nile red-loaded Gal-TMPDA (50 μg/ml) by normal and senescent 4T1 cells at 2, 4, 6, and 12 h post incubation with the nanoparticles. Nuclei, DAPI. Scale bar = 50 μm. (D) Flow cytometric analysis of the internalization of Nile red-loaded Gal-TMPDA by normal and senescent 4T1 cells that were incubated with the nanoparticles for 2, 4, 6, and 12 h, and (E) quantitative analysis of the fluorescence intensities of confocal images. (F) The effects of Gal-TMPDA@DQ at the indicated doses on the viability of 4T1 cells at 24 h and 48 h post treatment. (G) The effects of the indicated agents on the viability

of senescent 4T1 cells induced by Pab pretreatment (Free DQ (D: 2.87 µM, Q: 17.20 µM), MPDA (MPDA:100 µg/ml), TMPDA (TMPDA:100 µg/ml), Gal-MPDA@DQ (MPDA:100 µg/ml, D: 2.87 µM, Q: 17.20 µM), Gal-TMPDA@DQ (TMPDA:100 µg/ml, D: 2.87 µM, Q: 17.20 µM), Gal-MPDA@DQ/R (MPDA:100 µg/ml, D: 2.87 µM, Q: 17.20 µM), Gal-TMPDA@DQ/R (TMPDA:100 µg/ml, D: 2.87 µM, Q: 17.20 µM)). (H) Flow cytometry of cell apoptosis in senescent and normal 4T1 cells that were co-culture with the indicated agent (Free DQ (D: 2.87 µM, Q: 17.20 µM), MPDA (MPDA:100 µg/ml), TMPDA (TMPDA:100 µg/ml), Gal-MPDA@DQ (MPDA:100 µg/ml, D: 2.87 µM, Q: 17.20 µM), Gal-TMPDA@DQ (TMPDA:100 µg/ml, D: 2.87 µM, Q: 17.20 µM) , Gal-MPDA@DQ/R (MPDA:100 µg/ml, D: 2.87 µM, Q: 17.20 µM), Gal-TMPDA@DQ/R (TMPDA:100 µg/ml, D: 2.87 µM, Q: 17.20 µM)). for 24 h, and (I) quantification of the apoptosis rates. Data are from three independent experiments and presented as means ± SD. * P < 0.05, ** P < 0.01, *** P < 0.001, **** P < 0.0001.

Figure. 7. Gal-TMPDA@DQ targets Pab-induced senescent breast cancer in mice for specific clearance. (A, B) Orthotopic 4T1 breast cancers were established and grew till day 8. Mice were then treated with or without Pab daily for one week. The tumors were then collected for staining of SA-β-Gal (n= 3) (A), and immunohistochemistry staining with Ki67. Scale bar = 50 µm (n= 3) (B). (C-E) Breast cancer-bearing mice treated with or without Pab for one week as described in A, followed by the instillation of NR-loaded Gal-TMPDA (5 mg/ml, 200 µl) via tail vein. The nanoparticles were traced by IVIS system (Color Scale: Min = 1.20e8, Max = 1.40e9) at the indicated time periods (n= 3) (D), and the quantitation of the fluorescence were shown (n= 3) (E); The nanoparticles were traced by IVIS system (Color Scale: Min = 6.45e6, Max = 5.12e7) in tumors and major organs at the indicated time periods post nanoparticles inoculation (n= 3) (C). (F) Breast cancer-bearing mice treated with or without Pab for one week as described in A, followed by the administrated of Gal-MPDA@DQ or Gal-TMPDA@DQ for 24 h. The mice were then under the irradiation (808

nm, 1.0 W/cm^2) for the indicated time periods, and the infrared thermal images showing the photothermal convention capability of mice (n= 3). Data are presented as means ± SD. * P < 0.05, ** P < 0.01, *** P < 0.001, **** P < 0.0001.

Figure. 8. Gal-TMPDA@DQ/R promotes the removal of senescent tumor cells and inhibits tumor progression. (A-G) The simplified experimental scheme. Orthotopic 4T1 breast cancers were established and grew for 8 days (tumor volume increased to about 50 mm^3). The mice were then treated daily with Pab for 1 week to induce senescence, followed by the administration of PBS or the indicated therapeutic agents (Free DQ (D: 0.7mg/kg, Q: 2.6mg/kg), MPDA (5 mg/ml, 200 μl), TMPDA (5 mg/ml, 200 μl), MPDA@DQ (MPDA: 5 mg/ml, D: 70 μg/ml, Q: 260 μg/ml, 200 μl), TMPDA@DQ (TMPDA: 5 mg/ml, D: 70 μg/ml, Q: 260 μg/ml, 200 μl), MPDA@DQ/R (MPDA: 5 mg/ml, D: 70 μg/ml, Q: 260 μg/ml, 200 μl) or TMPDA@DQ/R (TMPDA: 5 mg/ml, D: 70 μg/ml, Q: 260 μg/ml, 200 μl)) for three times a Day 15, 18 and 21. Additionally, the mice receiving Gal-MPDA@DQ or Gal-TMPDA@DQ were also subjected to NIR exposure for three times on the next of the nanoparticle's inoculation. Mice were sacrificed 24 days for functional analysis. The body weights (n= 6) (B); Tumor volumes (n= 6) (C); Representative tumor tissues (n= 5) (D); TUNEL staining of tumor tissue sections. Nuclei, DAPI. Scale bar = 50 μm (n= 3) (E); Representative images of H&E staining of tumor tissues (scale bar =100 μm) (n= 3) (F), and lung tissue sections (scale bar = 200 μm) (n= 3) (G). Data are presented as means ± SD. * P < 0.05, ** P < 0.01, *** P < 0.001, **** P < 0.0001.

3. Discussion

Although the application of DQ has demonstrated the promising outcome in basic studies and clinical trials, the key issues such as non-optimized therapeutic efficacy, low biocompatibility, and off-target effects hinder its further utilization. In this study, we

developed an innovative nanoplatform to selectively and efficiently remove SnCs from diseased tissues while preserving healthy ones, thereby offering a potential treatment for age-related diseases. Specifically, we fabricated the PDA-based mesoporous nanostructures to encapsulate the senolytics DQ, by which the drug was delivered with high quantities, increased stability, and extend release otherwise it may be required several injections. To increase the selectivity of nanosenolytics, we further coated the nanoparticles with Galactan-modified shell to enable the drug release in a SA-β-gal-responsive manner (Pathway 2) (Graphical Abstract), preventing the drug diffusion to cause bilateral tissue injury. Furthermore, PTT was introduced into the nano system via TMPDA that combined with the canonical senolytics to exert the synergistic effects, thereby significantly improving the SnC-clearing effects. By exploiting the two mice models that are featured with SnCs deposition in the diseased tissues, we demonstrate that the newly developed nanosenolytics remarkably lessened SnC burdens and alleviated senescence-related pathologies, reversing lung fibrosis and halting cancer progression post therapy. Concurrently, no evident tissue damaging and blood toxicity were associated with the treatment. Thus, the present study develops a specific, efficient, and feasible nanosenolytics system, which show promise for treating age-related conditions with minimal toxicity concerns, paving the way for future trials for relevant diseases.

Relatively low therapeutic efficacy is a key hindrance for clinical application of canonical senolytic treatment. One solution for that is to increase the drug dose and administration times, which however would induce cytotoxicity to normal cells and potentially tissue injury. To resolve this issue, we herein take the advantage of PDA to fabricate the mesoporous framework with adjustable channels for enhanced intracellular accumulation and controlled release of the drug [39]. As crafting of the senolytics rely sensitively on the microstructure of nanospheres, it is essential to optimize the nanoparticle size and morphology, the pore

diameter, and drug functionalization. Our current study developed a unique system to assembly dopamine with the dual-soft-template (P123 and F127) in in an aqueous solution. To enlarge the pore size, we adjusted the P123/F127 mass ratio to extend the chain length of the surfactant templates, and TMB served as a welling agent to enter the hydrophobic interior of the micelles for the core enlargement [252, 40]. By this, we obtained small and evenly shaped particles with the distribution of the mesopores of 26 nm, much larger than that of conventional pores (3-4 nm) [41]. As increased pore size opens the possibility to adsorb larger guest molecules and reduce the biodegradation of the particles [42], our system thus provides a nanoplatform for stable and effective anchoring of DQ for the in vivo delivery.

An ideal therapeutic drug requires sustained drug release over an extended period to minimize the times of drug administration. While free DQ was reported to almost completely release within 8 h [43]. our data showed that release of D or Q from the nano spheroids lasted at least for 48 h. We observed that D and Q rapidly released from the micelle in the first 12 h and reached the release plateaus (about 40%) within 48 h (Figure 1H, I). Correlating with extended drug release, it was shown that the pulmonary physiology was greatly improved only on three treatments of the nanosenolytics. The dosage of DQ used in fibrotic mice (0.7 mg/kg D, 2.6 mg/kg Q) was much lower than that of pure DQ administrated in similar conditions (5 mg/kg D, 50 mg/kg Q) [35]. Moreover, lung physiology was confirmed to be improved at least 6 days after treatment, indicating the sustained benefits of senotherapy beyond the treatment period. We thus propose that the unique structure of mesoporous PDA with tunable channels provides a platform for stable encapsulation and extended release of DQ, making it possible to maximize the therapeutic efficacy of the senolytics at a relatively lower quantity.

Due to highly heterogeneity of SnCs in naturally aging organs or diseased tissues, it is hard to differentiate aging cells from normal cells. In this study, we exploit the MPDA

nanoparticles to conjugate the senolytics through π–π stacking and/or hydrogen bonding, the mechanism commonly utilized by PDA to bind drugs and chemical molecules [44]. Notably, the π–π interactions is sensitive to acid conditions owing to the protonation of amino groups on the PDA scaffolds [45]. Since SnCs are featured with low PH relative to normal cells, the PH responsiveness, along with SA-β-gal targeting strategy, greatly improves the SnC-specific effects of the nanosphere. As is known, lysosomal β-gal is increasingly expressed in SnCs and has been recognized as a hallmark of SnCs. In this study, we devised a galactose-modified bilayer to encapsulate the TMPDA nanosphere for the sequestration of DQ until the Galactan moiety is cleaved by lysosomal β-gal to release the drug. As proof-of-concept evidence, our data showed that the nanosenolytics were predominately located at lysosomes upon taken by SnCs (Figure 2D, E). Efficient release of D and Q was triggered by β-gal under acidic conditions, leading to the cytotoxic effect up to 80% in SnCs while mildly affecting the viability of non-senescent cells. Thus, the β-gal-responsive property endowed the nanosenolytics to precisely and efficiently kill the SnCs, which make it as a potential molecule for specific elimination of SnCs and treating age-related disorders [27, 46]. However, it should be noted that a single biomarker like SA-β-gal cannot represent the highly heterogeneous SnCs. Currently, a network of age-associated molecules including P53, P21 and P16, and the newly discovered senescence-related proteins such as dipeptidyl peptidase-4 (DPP4) [47], integrin $\alpha_v\beta_3$ [26a], glycoprotein nonmetastatic melanoma protein B (GPNMB) [48], and urokinase plasminogen activator receptor (uPAR) [49], are tested to be potential molecular targets for senotherapy. On the other hand, studies have shown that different cell subsets, as exemplified d by macrophages and lung epithelial cells in the pathogenesis of pulmonary fibrosis [50], have different roles in age-related pathologies and display distinct senescent biomarkers. Thus, association of multiple senescence markers and/or development of cell-specific signatures might be

required for designing more precise and smarter therapeutics that specifically targeting SnCs.

PTT is a non-invasive treatment that utilizes the photothermal agents (PTAs) to convert the absorbed photon energy into heat for killing targeted cells. Due to its excellent tissue penetration activity and photothermal conversion capability, NIR-driven PTT has been widely used in treating cancers, but is rarely applied in alleviating age-related disorders by targeting SnC. In this study, we demonstrated that compared with free DQ, Tempo-doped nanoparticles, upon NIR exposure, exhibited a strikingly improved effect in impeding cancer growth and metastasis after chemotherapy. This effect is largely through the photothermal conversion activity of the TMPDA nanoparticles, which boosted the release of DQ due to heat-enhanced molecule motion, and more importantly, exerted the additive cytotoxicity toward senescent cancer cells in combination of the senolytics. In this study, we devised a PTT system based on PDA, an organic material with excellent photothermal conversion ability. The incorporation of Tempo further enhances the light absorption capability and heat generating effects, leading to the temperature up to 61.9 ℃ and hence enhanced cytotoxicity. Of interest, traditional PTT exert thermal ablation of cancer cells by elevating the temperature above 48 °C, which however cause damage normal tissues and other adverse effects [51]. For this, the photothermal therapy with mild-temperature (42-45°C) is recently proposed to reduce unwanted cytotoxic effects, but it may compromise therapeutic efficacy [52]. Our current system took the advantage of TMPDA system to maximize the photothermal effects, and simultaneously, conquer the problems of heat diffusion and off-targeting effects by equipping the nanosenolytics with the SnC-targeting shell. More importantly, the integration of senolytics and PDA yields the synergistic effects, and remarkably increases the therapeutic efficacy as compared with either of the agent alone. Thus, we develop an all-

25

in-one multifunctional nanoplatform that specifically and robustly targeting senescent cancer cells for elimination.

On the other hand, therapy-induced senescence (TIS) occurs in both malignant and non-malignant cells following exposure to chemotherapy, which may serve as a holistic mechanism underpinning the age-related pathophysiology such as premature aging, fragile, cachexia and peripheral neuropathy [53]. TIS-targeting strategy is therefore expected to have additional health benefits by removing SnCs from normal tissues and counteracting the damaging effects associated with the treatments. As an example, a recently study revealed that a short anti-senescence intervention impeded the progression of radiation-induced frailty and disability in a pre-clinical setting [54]. In our current study, multiple tissues, including the brain, heart, liver and kidney, maintained functionality integrity after the senolytic treatment. Although a more thorough analysis is required, it is likely that administration of Gal-TMPDA@DQ may also eliminate SnCs in normal tissues upon intravenously administrated. This may lead to the so called "one stone two birds" effects, specifically, the senotherapy systemically removes SnCs and ameliorates therapy-induced premature frailty and morbidities in cancer survivors [55]. Future studies might be merited to further specify the health-improving efficacy of the nanosenolytics, or tailor the therapeutics to reduce the harmful impacts associated with traditional cancer treatments. Also, this study still has some limitations, specifically, β-Gal-directed senolytic strategy is not highly specific. Studies have shown that increased activity of SA-β-gal can also be observed in some types of cancer cells such as ovarian cancer cells, and it has been used as a diagnostic and therapeutic marker in treating cancers [56].Thus, the selectivity of Gal-TMPDA@DQ may be limited in some experimental models, and its therapeutic potential and possible toxicity need further evaluation.

4. Conclusion

In summary, our study develops a novel nanosenolytics that is characterized by a mesoporous framework with adjustable channel and smart surface modifications via the "double lock" mechanism combining Galactan layer and TMPDA. This system enables specific and efficient delivery of senolytic drugs and promotes the elimination of SnCs to improve age-related pathologies without severe adverse effects. The finding opens a new platform for the development of SnC-targeting therapeutics to delay aging or alleviate age-associated disorders.

5. Experimental Section

Determination of Dasatinib and Quercetin dosages

The dosage for oral administration of Dasatinib (D) in mice is 5 mg/kg[35], and the orally bioavailability of D is 14%[23]. Therefore, for intravenous injection of Dasatinib in mice, the dosage would be 0.7mg/kg. As for Quercetin (Q), the reference dosage for oral Q treatment in humans is 14.29mg/kg [13], and the oral bioavailability of Q in humans is 2% [57]. The human dosage of Q for intravenous injection would be 0.286 mg/kg. According to the pharmacological scaling formula, mouse dosage is equal to 9.1 times human dose. Therefore, the mice dosage of Q for intravenous injection would be 2.6 mg/kg.

Preparation of Gal-TMPDA@DQ and Gal-TMPDA@NR

TMPDA nanoparticles were synthesized as described previously [30, 58]. 30 mg of P123 (Pluronic® P-123, Sigma-Aldrich, 435465),75 mg of F127 (Pluronic® F-127, Sigma-Aldrich,

27

P2443),75 mg of DA (Dopamine hydrochloride, Macklin, D806618), 75 mg of Tempo (Macklin, T819129) were dissolved in 10 ml of 40% ethanol. The solution was subjected to ultrasonic dissolution, followed by the addition of 400 μl TMB (1,3,5-trimethylbenzene, Macklin, T818958) and 375 μl ammonium hydroxide solution (Macklin, A834475) with stirring at room temperature for 4h. The solution was then collected, centrifuged, and the supernatant was removed. The synthesized nanoparticles, termed TMPDA, were washed with ddH$_2$O and anhydrous ethanol and dried in a constant temperature oven at 60°C.

Next, TMPDA (1 mg/ml) were mixed with PEG-2000 (NH2-PEG-NH2, Aladdin, N590849) in aqueous solution (1:2). Dasatinib (D, 10 mg/ml, Sigma-Aldrich, SML2589) and Quercetin (Q, 26 mg/ml, Sigma-Aldrich, Q4951) in 0.2% DMSO were then added with stirring at room temperature for 12h in the dark, Galactan (BIOSYNTH, YG71532) was subsequently added at a ratio of 1:2 compared with TMPDA, and stirred for another 12h. Finally, the reaction solution was centrifuged and the precipitates were cleaned to obtain Gal-TMPDA@DQ. For tracing the nanoparticles, DQ were replaced by Nile red (NR, 10 mg/ml) to produce Gal-TMPDA@NR particles.

Morphological and physicochemical characterization of Gal-TMPDA@DQ

For examining the morphology of the nanoparticles, the nanoparticle solution (500 μg/ml) was drop-cast onto the carbon-coated copper grids, which were left to air-dry at room temperature. The morphology of the nanoparticles was observed by transmission electron microscope (TEM) (JEOL, Japan, JEM-1230). The size, Zeta potential, and stability of the nanoparticles were measured using Dynamic Light Scattering (DLS, Zetasizer Ultra, Malvern, UK).

For Molisch reaction, the solutions of Galactan (2 mg/ml) or Gal-TMPDA@DQ (5 mg/ml) were mixed with or without β-Gal (Shanghai Yanaye, S10066), in a pH 5.5 aqueous solution.

Drops of 5% α-naphthol (Macklin, N814571) were then added to the solution by gentle mixing. Subsequently, concentrated sulfuric acid was added along the tube walls to facilitate the formation of a layer and avoid mixing. The development of a purple ring at the layer is a positive indicator for Molisch's test.

Photothermal effects analysis

For testing the photothermal capability of Gal-TMPDA@DQ, a laser (Yuanming Laser, China, LSR808NL-2W-FC) with 808 nm near-infrared light was used for irradiation. The solution temperature was recorded by a digital thermometer. The photothermal conversion efficiency (η) is calculated according to the formula 1 and 2 [59].

$$\eta = \frac{hS(\Delta T_{max} - \Delta T_{max,H_2O})}{P(1 - 10^{-A})} \quad (1)$$

$$hS = \frac{mc + m'c'}{\tau} \quad (2)$$

h represents the heat transfer coefficient, and S means the surface area of the container, is the ΔT_{max} temperature change of the Gal-TMPDA@DQ solution at the maximum steady-state temperature, P is the laser power, A is the absorbance of Gal-TMPDA@DQ at 808 nm. hS value is calculated directly by formula 2, in which m, m', c, and c' are designated respectively as mass of Gal-TMPDA@DQ solution (0.1 g), the average mass of a single well of the 96-well plate (0.47 g), the heat capacity of nanomaterial solution (4.2 J/g °C) and the heat capacity of the 96-well plate (1.3 J/g °C). τ is the characteristic thermal time constant of the reaction, which can be calculated according to the relationship between temperature change and temperature decline rate during cooling. The infrared thermal imaging camera (UNI-T, China, Uti120S) was used to visualize the temperature changes caused by Gal-TMPDA@DQ at different concentrations within 5 min.

Measurement of drug loading capacity and encapsulation efficiency

In the preparation of Gal-TMPDA@DQ, the centrifuged supernatant was collected for UHPLC analysis. Simply put, after encapsulating Galactan onto the synthesized TMPDA@DQ nanoparticles, the unreacted solution was collected by centrifuging at 9500 rpm for 15 minutes. Later, an equal volume of aqueous solution was added to resuspend the collected solution, followed by repeating the centrifugation step. The supernatant wash solution was combined with the aforementioned unreacted solution to form the test solution. The chromatographic conditions were as follows: Column: C18-RP (Reverse Phase) column; Column temperature: 30 °C; Mobile phase: Methanol: H_2O = 7:3; Flow rate: 1 ml/min; Injection volume: 10 μl; Detection wavelengths: 321 nm for D, and 374 nm for Q. Drug loading (DL) and encapsulation efficiency (EE%) were calculated using the following formulas:

$$DL = \frac{\text{weight of feeding D or Q} - \text{drug concentration of supernatant} \times \text{volume}}{\text{The quality of Gal} - \text{TMPDA@DQ}} \quad (3)$$

$$EE\% = \frac{\text{weight of feeding D or Q} - \text{drug concentration of supernatant} \times \text{volume}}{\text{weight of feeding D or Q}} \times 100\% \quad (4)$$

Analysis of D and Q release

To measure the drug release rate, an equal volume of Gal-TMPDA@DQ solution was enclosed in a dialysis membrane (MW: 2000, Biosharp, BS-QT-021). The encapsulated samples were subjected to dialysis under PBS solutions (0.5 % SDS) at pH 7.4, and pH 5.5 respectively, with or without the addition of β-Gal. The release fluid (1 ml) from each group was collected at different time points and replenished with equivalent fresh buffer solution. The collected release fluid was analyzed for drug concentration using UPLC. Alternatively, the samples were under near-infrared irradiation (NIR, 808 nm, 1.0 W/cm^2) for 3 min.

Induction of SnCs

For induction of SnCs, A549 cells were stimulated with 0.01 U/ml bleomycin (Sigma-Aldrich, 203401) for 2 days [60]. 4T1 cells were treated with 5 µM palbociclib (Sigma-Aldrich, PZ0383) for 2 weeks [38].

Mice fibrosis and chemotherapy-induced senescence models

Animal experiments were performed according to the NIH Guide for the Care and Use of Laboratory Animals, with the approval of the Scientific Investigation Board of Zhejiang Laboratory Animal Center (ZJCLA-IACUC-20010687). All mice in our experiments were gender and age matched. For IPF model, male C57BL/6 mice at the age of 8-10 weeks were intratracheally administered with bleomycin (2 U/kg) under isoflurane anesthesia [35]. Alternatively, the mice receiving Bleo were further administrated with the nanoparticles or vehicles intravenously at day 6, 12, 18. Mice were sacrificed at day 24. Lung fibrosis and age-associated pathologies were assessed.

For establishing the breast cancer model, female Balb/c mice at the age of 6-8 weeks were injected with 0.5×10^6 4T1 cells at the mammary fat pads on day 0. Starting from day 8, palbociclib (100 mg/kg) was orally administrated for 7 consecutive days [38]. to induce senescence. The mice were then injected intravenously with the nanoparticles at Day 15, 18 and 21, and alternatively, the mice were also subjected to NIR (808 nm, 1.0 W/cm^2, 300 s) exposure at the next day. Tumor weights were measured every three days and mice were sacrificed at day 24 for analysis.

Examination of cellular internalization of nanoparticles

Briefly, cells were co-incubated with the nanoparticles loaded with Nile red (NR), and collected at 2, 4, 6, and 12 h. Cells were then fixed with 4% paraformaldehyde, and

visualized by AXIO Observe Inverted Fluorescence Microscope (Zeiss, Germany). Cell nuclei were stained with 4', 6-diamidino-2-phenylindole (DAPI, Beyotime, C1002). For measuring the fluorescence intensities, cells were analyzed by a flow cytometer (FACSCanto II, BD, USA).

For detecting the lysosome-targeting property of the nanoparticles, cells taking the NR-loaded nanoparticles were incubated with Lyso-tracker Green (Beyotime, C1047S) for 30 min, washed and fixed with 4% paraformaldehyde. Colocalization of NR-nanoparticles and Lyso-tracker Green was detected by a confocal microscope (Zeiss, LSM980, Germany).

Cell viability assay

A549 and 4T1 cells were seeded at a density of 8×10^3 cells per well in a 96-well plate overnight and incubated with different concentrations of the nanoparticles for 24 h. Cells with the vehicle were used as a control. Then, the medium was discarded and serum-Free medium containing 10μl of CCK8 solution (Cell Counting Kit-8, Beyotime, C0038) was added into each well, followed by incubation at 37°C for 2 h. The absorbance at 450 nm was measured using Multiskan SkyHigh full-wavelength microplate reader (Thermo Scientific™, A51119500C).

Apoptosis assay

A549 and 4T1 cells (1×10^5) were treated with the nanoparticles, and also NIR (808 nm, 1.0 W/cm^2, 300 s) exposure in some conditions. 24 h later, cells were collected and stained with Annexin V-FITC/propidium iodide (Beyotime, C1062L, China), followed by the analysis of flow cytometry.

β-galactosidase detection

A549 or 4T1 cells, frozen lung tissue sections or tumor tissues were fixed with 4% paraformaldehyde for 15 min, and then stained for SA-β-gal using the Senescence Cells Histochemical Staining Kit (Beyotime, C0602) according to the manufacturer's instructions.

In vivo imaging of the nanoparticles in IPF mice and tumor-bearing mice

Firstly, for tumor-bearing mice were implanted with 4T1 cells as descried as above, and treated with or without Pab for 7 days, for IPF mice were treated with bleomycin for 7 days.

IPF mice and tumor-bearing mice were then intravenously injected with 200 μl of 5 mg/ml Gal-TMPDA@NR, and imaged by the IVIS system (IVIS Lumina, USA) at 3, 6, 12, 24, and 48 h. Alternatively, major organs (tumor, heart, liver, spleen, lung, and kidney) were collected for tracking the nanoparticles at different time points.

Cytokines analysis in bronchoalveolar lavage fluid (BALF)

Briefly, mice were anesthetized and their tracheae were exposed through the midline and cannulated with a sterile needle (1mL). Bronchoalveolar lavage fluid (BALF) was obtained by flushing the lungs three times with 1 mL EDTA/PBS (0.5 mM) [61]. After centrifugation, BALF supernatants were stored at -80°C for use. The levels of TNF-α (Mouse TNF Alpha ELISA Kit, Boster, EK0527), IL-1β (Mouse IL-1β ELISA Kit, Boster, EK0394), IL-6 (Mouse IL-6 ELISA Kit, Boster, EK0411), and IL-10 (Mouse IL-10 ELISA Kit, Boster, EK0417) in the BALF were determined by ELISA.

Hydroxyproline assay

Total left lung was collected in each mouse and washed with cold PBS. Quantification of hydroxyproline was performed by Hydroxyproline Content Assay Kit (Solarbio, BC0250) according to manufacturer's instructions.

Histological staining

The tissue samples were fixed in 4% paraformaldehyde, paraffin-embedded, and sectioned into 4-μm-thin slices. The slides were then deparaffinized and rehydrated, followed by staining with hematoxylin and eosin (Beyotime, C0105M), or Masson's Trichrome (Solarbio, G1340).

For immunohistochemical staining, the sections from formalin-fixed, paraffin-embedded tissue samples were routinely deparaffinized and rehydrated. Endogenous peroxidase was quenched by incubation with 3% hydrogen peroxide in 97% methanol, and the antigens were retrieved with a 0.01 M citrate buffer at pH 6. The slides were subsequently incubated with rabbit-anti Ki67 (1:200, abcam, ab16667), rabbit-anti α-SMA (1:200, Affinity Biosciences, AF1032), Rabbit-anti γ-H2A.X (1:200, CST, 9718T) for 2 h. After washing completely, the slides were incubated with HRP-conjugated goat anti-Rabbit IgG (1:1000, abcam, AB205718), and DAB (3, 3'-Diaminobenzidine) was used a chromogen. The sections were subsequently counterstained with Meyer's hematoxylin (Merck, Darmstadt, Germany), or the slides were incubated with Alexa Fluor® 488-conjugated goat anti-Rabbit IgG (1:1000, abcam, ab150077), and DAPI was used to stain the nucleus. Digital slide scanning was performed using a slide scanner (Ningbo Shunyu, China).

TUNEL staining

The deparaffinized sections were incubated in proteinase K for 10 min, and washed three times in PBS. TUNEL staining was performed according to the manufactures' guidance (RecordBio, RCT-50G). Nuclei were counterstained with DAPI (1:500), and digital slide scanning was performed.

Quantitative real-time PCR (qPCR)

Total RNA was extracted from either cell lysate or snap-frozen lungs with TRIzol reagent. The cDNA was obtained using a HiScript® II Q RT SuperMix (gDNA wiper, Vazyme, R222-01) according to the manufacturer's instructions. The qRT-PCR gene expression analysis was performed using SYBR Green Premix Pro Taq HS qPCR Kit (Accurate Biology, AG11701). qRT-PCR data were normalized to β-actin as a housekeeping standard. Fold changes of target mRNAs were analyzed using the $2^{-\Delta\Delta CT}$ method.

Western blot

Cells or quick-frozen lungs were incubated in lysis buffer (1% Triton X-100, 1% deoxycholate, 0.1% NaN_3) containing protease inhibitor cocktail tablets (Roche Diagnostics). Equal volumes of the samples were separated by 10 % SDS-polyacrylamide gel electrophoresis [62]. The separated proteins were then transferred to a polyvinylidene difluoride membrane and blocked with 5% skim milk. The membranes were then incubated overnight with the primary antibodies, followed by incubation with appropriate secondary antibodies conjugated to horseradish peroxidase (Santa Cruz Biotechnology, Dallas, TX, USA). Electrochemiluminescence chromogenic substrate was added to visualize the target bands using a ChemiDoc imaging system (Bio-Rad, USA).

The antibodies used in the immunoblotting include: mouse anti-P53 (1:500, Santa Cruz, sc-126), mouse anti-CDKN1A/P21 (1:500, Santa Cruz, sc-6246), mouse anti-CDKN2A/P16 (1:500, Santa Cruz, sc-1661), mouse anti-GAPDH (1:1000, Santa Cruz, sc-365062), HRP-conjugated horse anti-mouse IgG (1:1000, CST, 7076S).

Hemolysis assay in vitro

100 μl of Gal-TMPDA@DQ (5 mg/ml) was added to 900 μl of 2% red blood cell suspension. Distilled water and saline were used as positive and negative controls,

respectively. After incubation at 37°C for 5 min, the samples were centrifuged at 8000 rpm for 5 min, and the photographs of the hemolysis in each tube were taken. Also, the supernatants were collected, and the absorbance was measured at 541 nm. The hemolysis rate was calculated as follows:

Hemolysis (%) = (A-C)/(B-C) × 100%

Where A, B, and C represented the absorbance of the sample, the positive control, and the negative control, respectively [63].

Examination of tissue toxicity

The major organs were collected, fixed, dehydrated, and paraffin-embedded routinely, and the prepared sections were then stained with H&E for histological examination.

To detect the liver and kidney functions, murine blood was collected in the anti-coagulant tubes containing sodium heparin and divided into two portions. One portion was analyzed for HGB/PLT/RBC/WBC indexes using an automated hematology analyzer (TECOM, TEK8500-VET). The other half of the blood was centrifuged at 3000g, 4°C to obtain the plasma, which was then to measure mouse ALT (MEIMIAN, MM-0260M1), AST (MEIMIAN, MM-44115M1), and BUN (MEIMIAN, MM-0692M1) levels.

Statistical analysis

All results are analyzed using GraphPad Prism software (version 8.2.1) and expressed as means ± SD. Statistical analyses were performed using a one- or two-tailed unpaired t-test or a one-way analysis of variance (ANOVA) to evaluate differences between groups. Differences were considered statistically significant at $P < 0.05$. *$P < 0.05$, **$P < 0.01$, ***$P < 0.001$, and ****$P < 0.0001$. Representative images from at least three independent

experiments or animals were shown, and the quantitative image analysis was conducted using ImageJ software.

Supporting Information

Supporting Information is available from the Wiley Online Library or from the author.

Acknowledgements

Conflict of Interest

The authors declare no competing interests.

Author Contributions

L. S. and X. X. conceived the experiments, and supervised the study. H. Z., W. L., C. J., C. C. C. Z. and W. G. performed the experiments, analyzed the data, and prepared the manuscript. X. S. provided insightful suggestions. L. S., X. X. and H. Z wrote and revised the manuscript.

Data Availability Statement

The data that support the findings of this study are available in the supplementary material of this article.

References and Notes

[1] E. R. A, P. N. B, A. P. B, B. M. B, R. S. A, M. G. A, *Maturitas* **2020**, 139, 6.

[2] R. Di Micco, V. Krizhanovsky, D. Baker, F. d'Adda di Fagagna, *Nat Rev Mol Cell Biol* **2021**, 22, 75.

[3] a)L. Delval, A. Hantute-Ghesquier, V. Sencio, J. M. Flaman, C. Robil, F. S. Angulo, L. Lipskaia, O. Çobanoğlu, A. S. Lacoste, A. Machelart, A. Danneels, M. Corbin, L. Deruyter, S. Heumel, T. Idziorek, K. Séron, F. Sauve, A. Bongiovanni, V. Prévot, I. Wolowczuk, S. Belouzard, J. M. Saliou, P. Gosset, D. Bernard, Y. Rouillé, S. Adnot, M. Duterque-Coquillaud, F. Trottein, *Nat Aging* **2023**, 3, 829; b)B. G. Childs, M. Durik, D. J. Baker, J. M. van Deursen, *Nat Med* **2015**, 21, 1424.

[4] D. J. Baker, T. Wijshake, T. Tchkonia, N. K. LeBrasseur, B. G. Childs, B. van de Sluis, J. L. Kirkland, J. M. van Deursen, *Nature* **2011**, 479, 232.

[5] Y. Zhu, T. Tchkonia, T. Pirtskhalava, A. C. Gower, H. Ding, N. Giorgadze, A. K. Palmer, Y. Ikeno, G. B. Hubbard, M. Lenburg, S. P. O'Hara, N. F. LaRusso, J. D. Miller, C. M. Roos, G. C. Verzosa, N. K. LeBrasseur, J. D. Wren, J. N. Farr, S. Khosla, M. B. Stout, S. J. McGowan, H. Fuhrmann-Stroissnigg, A. U. Gurkar, J. Zhao, D. Colangelo, A. Dorronsoro, Y. Y. Ling, A. S. Barghouthy, D. C. Navarro, T. Sano, P. D. Robbins, L. J. Niedernhofer, J. L. Kirkland, *Aging Cell* **2015**, 14, 644.

[6] J. Chang, Y. Wang, L. Shao, R. M. Laberge, M. Demaria, J. Campisi, K. Janakiraman, N. E. Sharpless, S. Ding, W. Feng, Y. Luo, X. Wang, N. Aykin-Burns, K. Krager, U. Ponnappan, M. Hauer-Jensen, A. Meng, D. Zhou, *Nat Med* **2016**, 22, 78.

[7] H. Fuhrmann-Stroissnigg, Y. Y. Ling, J. Zhao, S. J. McGowan, Y. Zhu, R. W. Brooks, D. Grassi, S. Q. Gregg, J. L. Stripay, A. Dorronsoro, L. Corbo, P. Tang, C. Bukata, N. Ring, M. Giacca, X. Li, T. Tchkonia, J. L. Kirkland, L. J. Niedernhofer, P. D. Robbins, *Nat Commun* **2017**, 8, 422.

[8] A. Guerrero, N. Herranz, B. Sun, V. Wagner, S. Gallage, R. Guiho, K. Wolter, J. Pombo, E. E. Irvine, A. J. Innes, J. Birch, J. Glegola, S. Manshaei, D. Heide, G. Dharmalingam, J. Harbig, A.

Olona, J. Behmoaras, D. Dauch, A. G. Uren, L. Zender, S. Vernia, J. P. Martínez-Barbera, M. Heikenwalder, D. J. Withers, J. Gil, *Nat Metab* **2019**, 1, 1074.

[9] Q. Xu, Q. Fu, Z. Li, Y. Sun, *Nature Metabolism* **2021**.

[10] J. N. Farr, M. Xu, M. M. Weivoda, D. G. Monroe, D. G. Fraser, J. L. Onken, B. A. Negley, J. G. Sfeir, M. B. Ogrodnik, C. M. Hachfeld, N. K. LeBrasseur, M. T. Drake, R. J. Pignolo, T. Pirtskhalava, T. Tchkonia, M. J. Oursler, J. L. Kirkland, S. Khosla, *Nat Med* **2017**, 23, 1072.

[11] C. M. Roos, B. Zhang, A. K. Palmer, M. B. Ogrodnik, T. Pirtskhalava, N. M. Thalji, M. Hagler, D. Jurk, L. A. Smith, G. Casaclang-Verzosa, Y. Zhu, M. J. Schafer, T. Tchkonia, J. L. Kirkland, J. D. Miller, *Aging Cell* **2016**, 15, 973.

[12] M. M. Gonzales, V. R. Garbarino, T. F. Kautz, J. P. Palavicini, M. Lopez-Cruzan, S. K. Dehkordi, J. J. Mathews, H. Zare, P. Xu, B. Zhang, C. Franklin, M. Habes, S. Craft, R. C. Petersen, T. Tchkonia, J. L. Kirkland, A. Salardini, S. Seshadri, N. Musi, M. E. Orr, *Nat Med* **2023**, 29, 2481.

[13] L. J. Hickson, L. G. P. Langhi Prata, S. A. Bobart, T. K. Evans, N. Giorgadze, S. K. Hashmi, S. M. Herrmann, M. D. Jensen, Q. Jia, K. L. Jordan, T. A. Kellogg, S. Khosla, D. M. Koerber, A. B. Lagnado, D. K. Lawson, N. K. LeBrasseur, L. O. Lerman, K. M. McDonald, T. J. McKenzie, J. F. Passos, R. J. Pignolo, T. Pirtskhalava, I. M. Saadiq, K. K. Schaefer, S. C. Textor, S. G. Victorelli, T. L. Volkman, A. Xue, M. A. Wentworth, E. O. Wissler Gerdes, Y. Zhu, T. Tchkonia, J. L. Kirkland, *EBioMedicine* **2019**, 47, 446.

[14] L. Wang, B. Wang, N. S. Gasek, Y. Zhou, R. L. Cohn, D. E. Martin, W. Zuo, W. F. Flynn, C. Guo, E. R. Jellison, T. Kim, L. Prata, A. K. Palmer, M. Li, C. L. Inman, L. S. Barber, I. M. A. Al-Naggar, Y. Zhou, W. Du, Kshitiz, G. A. Kuchel, A. Meves, T. Tchkonia, J. L. Kirkland, P. Robson, M. Xu, *Cell Metab* **2022**, 34, 75.

[15] a)J. N. Justice, A. M. Nambiar, T. Tchkonia, N. K. LeBrasseur, R. Pascual, S. K. Hashmi, L. Prata, M. M. Masternak, S. B. Kritchevsky, N. Musi, J. L. Kirkland, *EBioMedicine* **2019**, 40, 554; b)A. Nambiar, D. Kellogg, 3rd, J. Justice, M. Goros, J. Gelfond, R. Pascual, S. Hashmi, M. Masternak, L. Prata, N. LeBrasseur, A. Limper, S. Kritchevsky, N. Musi, T. Tchkonia, J. Kirkland, *EBioMedicine* **2023**, 90, 104481.

[16] a)H. Power, P. Valtchev, F. Dehghani, A. Schindeler, *Aging Cell* **2023**, 22, e13948; b)N. S. Gasek, G. A. Kuchel, J. L. Kirkland, M. Xu, *Nat Aging* **2021**, 1, 870.
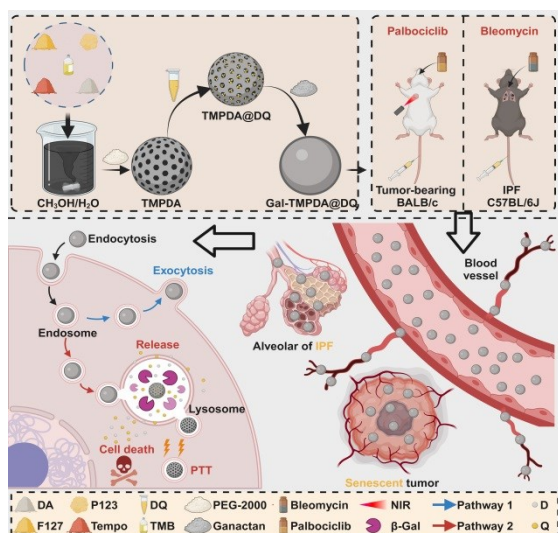
[17] M. P. Baar, R. M. C. Brandt, D. A. Putavet, J. D. D. Klein, K. W. J. Derks, B. R. M. Bourgeois, S. Stryeck, Y. Rijksen, H. van Willigenburg, D. A. Feijtel, I. van der Pluijm, J. Essers, W. A. van Cappellen, I. W. F. van, A. B. Houtsmuller, J. Pothof, R. W. F. de Bruin, T. Madl, J. H. J. Hoeijmakers, J. Campisi, P. L. J. de Keizer, *Cell* **2017**, 169, 132.

[18] T. D. Admasu, K. Kim, M. Rae, R. Avelar, R. L. Gonciarz, A. Rebbaa, J. Pedro de Magalhães, A. R. Renslo, A. Stolzing, A. Sharma, *Cell Rep* **2023**, 42, 112058.

[19] A. Hamadi, A. P. Grigg, G. Dobie, K. L. Burbury, A. P. Schwarer, F. A. Kwa, D. E. Jackson, *Thromb Haemost* **2019**, 119, 1112.

[20] C. Guignabert, C. Phan, A. Seferian, A. Huertas, L. Tu, R. Thuillet, C. Sattler, M. Le Hiress, Y. Tamura, E. M. Jutant, M. C. Chaumais, S. Bouchet, B. Manéglier, M. Molimard, P. Rousselot, O. Sitbon, G. Simonneau, D. Montani, M. Humbert, *J Clin Invest* **2016**, 126, 3207.

[21] a)M. Raffaele, K. Kovacovicova, J. Frohlich, O. Lo Re, S. Giallongo, J. A. Oben, M. Faldyna, L. Leva, A. G. Giannone, D. Cabibi, M. Vinciguerra, *Cell Commun Signal* **2021**, 19, 44; b)M. Raffaele, M. Vinciguerra, *Lancet Healthy Longev* **2022**, 3, e67.

[22] M. Ogrodnik, S. Miwa, T. Tchkonia, D. Tiniakos, C. L. Wilson, A. Lahat, C. P. Day, A. Burt, A. Palmer, Q. M. Anstee, S. N. Grellscheid, J. H. J. Hoeijmakers, S. Barnhoorn, D. A. Mann, T. G. Bird, W. P. Vermeij, J. L. Kirkland, J. F. Passos, T. von Zglinicki, D. Jurk, *Nat Commun* **2017**, 8, 15691.

[23] A. V. Kamath, J. Wang, F. Y. Lee, P. H. Marathe, *Cancer Chemother Pharmacol* **2008**, 61, 365.

[24] X. Bao, J. Zhao, J. Sun, M. Hu, X. Yang, *ACS Nano* **2018**, 12, 8882.

[25] a)Z. Cao, X. Liu, W. Zhang, K. Zhang, L. Pan, M. Zhu, H. Qin, C. Zou, W. Wang, C. Zhang, Y. He, W. Lin, Y. Zhang, D. Han, M. Li, J. Gu, *ACS Nano* **2023**, 17, 23746; b)R. Narayan, U. Y. Nayak, A. M. Raichur, S. Garg, *Pharmaceutics* **2018**, 10.

[26] a)S. Kim, J. B. Chae, D. Kim, C. W. Park, Y. Sim, H. Lee, G. Park, J. Lee, S. Hong, B. Jana, C. Kim, H. Chung, J. H. Ryu, *J Am Chem Soc* **2023**, 145, 21991; b)C. Amor, J. Feucht, J. Leibold, Y. J. Ho, C. Zhu, D. Alonso-Curbelo, J. Mansilla-Soto, J. A. Boyer, X. Li, T. Giavridis, A. Kulick, S. Houlihan, E. Peerschke, S. L. Friedman, V. Ponomarev, A. Piersigilli, M. Sadelain, S. W. Lowe, *Nature* **2020**, 583, 127.

[27] a)D. Shi, W. Liu, Y. Gao, X. Li, Y. Huang, X. Li, T. D. James, Y. Guo, J. Li, *Nat Aging* **2023**, 3, 297; b)Y. Cai, H. Zhou, Y. Zhu, Q. Sun, Y. Ji, A. Xue, Y. Wang, W. Chen, X. Yu, L. Wang, H. Chen, C. Li, T. Luo, H. Deng, *Cell Res* **2020**, 30, 574.

[28] a)M. Chang, Y. Dong, H. Xu, A. B. Cruickshank-Taylor, J. S. Kozora, B. Behpour, W. Wang, *Angew Chem Int Ed Engl* **2024**, 63, e202315425; b)W. Ji, H. Zhou, W. Liang, W. Zhang, B. Gong, T. Yin, J. Chu, J. Zhuang, J. Zhang, Y. Luo, Y. Liu, J. Gao, Y. Yin, *Small* **2024**, e2308574.

[29] A. A. Parkhitko, E. Filine, M. Tatar, *Nat Aging* **2023**, 3, 1187.

[30] Y. Zou, X. Chen, P. Yang, G. Liang, Y. Yang, Z. Gu, Y. Li, *Sci Adv* **2020**, 6.

[31] S. Freed, K. M. Sancier, *Science* **1953**, 117, 655.

[32] A. J. Podolanczuk, A. W. Wong, S. Saito, J. A. Lasky, C. J. Ryerson, O. Eickelberg, *Am J Respir Crit Care Med* **2021**, 203, 1343.

[33] K. Aoshiba, T. Tsuji, A. Nagai, *Eur Respir J* **2003**, 22, 436.

[34] Y. Enomoto, H. Katsura, T. Fujimura, A. Ogata, S. Baba, A. Yamaoka, M. Kihara, T. Abe, O. Nishimura, M. Kadota, D. Hazama, Y. Tanaka, Y. Maniwa, T. Nagano, M. Morimoto, *Nat Commun* **2023**, 14, 4956.

[35] M. J. Schafer, T. A. White, K. Iijima, A. J. Haak, G. Ligresti, E. J. Atkinson, A. L. Oberg, J. Birch, H. Salmonowicz, Y. Zhu, D. L. Mazula, R. W. Brooks, H. Fuhrmann-Stroissnigg, T. Pirtskhalava, Y. S. Prakash, T. Tchkonia, P. D. Robbins, M. C. Aubry, J. F. Passos, J. L. Kirkland, D. J. Tschumperlin, H. Kita, N. K. LeBrasseur, *Nat Commun* **2017**, 8, 14532.

[36] S. Cang, C. Iragavarapu, J. Savooji, Y. Song, D. Liu, *J Hematol Oncol* **2015**, 8, 129.

[37] C. A. Schmitt, B. Wang, M. Demaria, *Nat Rev Clin Oncol* **2022**, 19, 619.

[38] B. Lozano-Torres, J. F. Blandez, I. Galiana, A. García-Fernández, M. Alfonso, M. D. Marcos, M. Orzáez, F. Sancenón, R. Martínez-Máñez, *Angew Chem Int Ed Engl* **2020**, 59, 15152.

[39] a)B. Y. Guan, S. L. Zhang, X. W. D. Lou, *Angew Chem Int Ed Engl* **2018**, 57, 6176; b)B. Xu, S. Li, R. Shi, H. Liu, *Signal Transduct Target Ther* **2023**, 8, 435.

[40] Z. Li, Y. Yan, M. Liu, Z. Qu, Y. Yue, T. Mao, S. Zhao, M. Liu, Z. Lin, *Proc Natl Acad Sci U S A* **2023**, 120, e2218261120.

[41] M. Kresge, W. Leonowicz, J. Roth, J. Vartuli, **1992**.

[42] a)T. Ghosh, M. Mantri, Z. Gu, M. Kalantari, M. Yu, C. Yu, *J Mater Chem B* **2018**, 6, 763; b)K. Zhang, L. L. Xu, J. G. Jiang, N. Calin, K. F. Lam, S. J. Zhang, H. H. Wu, G. D. Wu, B. Albela, L. Bonneviot, P. Wu, *J Am Chem Soc* **2013**, 135, 2427.

[43] X. Chen, L. Zhang, X. Shao, W. Gong, T. Shi, J. Dong, Y. Shi, S. Shen, Y. He, J. Qin, *Advanced functional materials* **2022**, 32.

[44] F. Chen, Y. Xing, Z. Wang, X. Zheng, J. Zhang, K. Cai, *Langmuir* **2016**, 32, 12119.

[45] X. Wang, J. Zhang, Y. Wang, C. Wang, J. Xiao, Q. Zhang, Y. Cheng, *Biomaterials* **2016**, 81, 114.

[46] a)Y. He, L. Zhang, X. Chen, B. Liu, X. Shao, D. Fang, J. Lin, N. Liu, Y. Lou, J. Qin, Q. Jiang, B. Guo, *Adv Healthc Mater* **2023**, e2302972; b)S. Ni, Q. Liu, X. Chen, L. Ding, L. Cai, F. Mao, D. Shi, R. M. Hoffman, J. Li, L. Jia, *Signal Transduct Target Ther* **2022**, 7, 313.

[47] R. Zhao, X. Jin, A. Li, B. Xu, Y. Shen, W. Wang, J. Huang, Y. Zhang, X. Li, *Adv Sci (Weinh)* **2022**, 9, e2104128.

[48] M. Suda, I. Shimizu, G. Katsuumi, Y. Yoshida, Y. Hayashi, R. Ikegami, N. Matsumoto, Y. Yoshida, R. Mikawa, A. Katayama, J. Wada, M. Seki, Y. Suzuki, A. Iwama, H. Nakagami, A. Nagasawa, R. Morishita, M. Sugimoto, S. Okuda, M. Tsuchida, K. Ozaki, M. Nakanishi-Matsui, T. Minamino, *Nat Aging* **2021**, 1, 1117.

[49] C. Amor, I. Fernández-Maestre, S. Chowdhury, Y. J. Ho, S. Nadella, C. Graham, S. E. Carrasco, E. Nnuji-John, J. Feucht, C. Hinterleitner, V. J. A. Barthet, J. A. Boyer, R. Mezzadra, M. G. Wereski, D. A. Tuveson, R. L. Levine, L. W. Jones, M. Sadelain, S. W. Lowe, *Nat Aging* **2024**.

[50] M. Lehmann, M. Korfei, K. Mutze, S. Klee, W. Skronska-Wasek, H. N. Alsafadi, C. Ota, R. Costa, H. B. Schiller, M. Lindner, D. E. Wagner, A. Günther, M. Königshoff, *Eur Respir J* **2017**, 50.

[51] X. Yi, Q. Y. Duan, F. G. Wu, *Research (Wash D C)* **2021**, 2021, 9816594.

[52] K. Li, K. Xu, S. Liu, Y. He, M. Tan, Y. Mao, Y. Yang, J. Wu, Q. Feng, Z. Luo, K. Cai, *ACS Nano* **2023**, 17, 20218.

[53] a)M. Alsalem, A. Ellaithy, S. Bloukh, M. Haddad, T. Saleh, *Support Care Cancer* **2024**, 32, 85; b)D. A. Englund, A. M. Jolliffe, G. J. Hanson, Z. Aversa, X. Zhang, X. Jiang, T. A. White, L. Zhang, D. G. Monroe, P. D. Robbins, L. J. Niedernhofer, T. M. Kamenecka, S. Khosla, N. K. LeBrasseur, *JCI Insight* **2024**, 9.

[54] E. Fielder, T. Wan, G. Alimohammadiha, A. Ishaq, E. Low, B. M. Weigand, G. Kelly, C. Parker, B. Griffin, D. Jurk, V. I. Korolchuk, T. von Zglinicki, S. Miwa, *Elife* **2022**, 11.

[55] a)M. Xu, T. Pirtskhalava, J. N. Farr, B. M. Weigand, A. K. Palmer, M. M. Weivoda, C. L. Inman, M. B. Ogrodnik, C. M. Hachfeld, D. G. Fraser, J. L. Onken, K. O. Johnson, G. C. Verzosa, L. G. P. Langhi, M. Weigl, N. Giorgadze, N. K. LeBrasseur, J. D. Miller, D. Jurk, R. J. Singh, D. B. Allison, K. Ejima, G. B. Hubbard, Y. Ikeno, H. Cubro, V. D. Garovic, X. Hou, S. J. Weroha, P. D. Robbins, L. J. Niedernhofer, S. Khosla, T. Tchkonia, J. L. Kirkland, *Nat Med* **2018**, 24, 1246; b)J. Meng, Y. Li, C. Wan, Y. Sun, X. Dai, J. Huang, Y. Hu, Y. Gao, B. Wu, Z. Zhang, K. Jiang, S. Xu, J. F. Lovell, Y. Hu, G. Wu, H. Jin, K. Yang, *JCI Insight* **2021**, 6.

[56] Q. Yu, L. Zhang, M. Jiang, L. Xiao, Y. Xiang, R. Wang, Z. Liu, R. Zhou, M. Yang, C. Li, M. Liu, X. Zhou, S. Chen, *Angew Chem Int Ed Engl* **2023**, 62, e202313137.

[57] Y. Li, J. Yao, C. Han, J. Yang, M. T. Chaudhry, S. Wang, H. Liu, Y. Yin, *Nutrients* **2016**, 8, 167.

[58] X. Zhou, J. Liang, Q. Liu, D. Huang, J. Xu, H. Gu, W. Xue, *Int J Pharm* **2021**, 592, 120020.

[59] W. Ren, Y. Yan, L. Zeng, Z. Shi, A. Gong, P. Schaaf, D. Wang, J. Zhao, B. Zou, H. Yu, G. Chen, E. M. Brown, A. Wu, *Adv Healthc Mater* **2015**, 4, 1526.

[60] H. Cui, N. Xie, S. Banerjee, T. Dey, R. M. Liu, V. B. Antony, Y. Y. Sanders, T. S. Adams, J. L. Gomez, V. J. Thannickal, N. Kaminski, G. Liu, *Am J Respir Crit Care Med* **2022**, 206, 459.

[61] N. Lv, Y. Zhao, X. Liu, L. Ye, Z. Liang, Y. Kang, Y. Dong, W. Wang, N. Kolliputi, L. Shi, *Aging Cell* **2022**, 21, e13594.

[62] W. Zhang, Q. Han, Y. Ding, H. Zhou, Z. Chen, J. Wang, J. Xiang, Z. Song, M. Abbas, L. Shi, *Cell Mol Life Sci* **2022**, 80, 14.

[63] R. K. O'Leary, W. L. Guess, *Journal of Pharmaceutical ences* **2010**, 57, 12.

A "double lock and key" switchable nanoplatform that responds to senescent cells is developed. The release of dasatinib and quercetin within senescent cells is opened by the activation of β-galactosidase, low pH, and photothermal therapy, thereby selectively killing senescent cells. This approach has been shown to reverse pulmonary fibrosis and prevent the growth and metastasis of breast cancer.